

High-Performance Planar Isolated Current Sensor for Power Electronics Applications

Luca Dalessandro, *Student Member, IEEE*, Nicolas Karrer, *Member, IEEE*, and Johann W. Kolar, *Senior Member, IEEE*

Abstract—A planar current sensor, comprised of a magnetic current transformer and a Hall-effect element, is presented. The sensor has a broad frequency bandwidth from dc up to 30 MHz, a high current rating (40-A dc), superior linearity, high EMI immunity, small size, robustness, and low realization cost. The main design formulations are given analytically; simulations and finite-element results are presented for verification. Experimental results of current step response and dv/dt immunity are included.

Index Terms—Current measurement, current transformer, Hall-effect sensor, permeance-capacitance analogy.

I. INTRODUCTION

INDUSTRIAL electronics equipments for measurement [1], control [2], protection [3] and diagnostics [4] often require high-performance current sensors with features such as:

- 1) wide frequency bandwidth;
- 2) high current rating;
- 3) high dv/dt immunity;
- 4) linearity and stability with temperature variations;
- 5) compatibility with integration processes;
- 6) low realization effort and low cost.

The types of current sensors that have appeared in recent publications were based on numerous different physical effects, for instance magnetic coupling [5]–[7], magneto resistance [8], [9], Faraday induction [10], Hall effect [11], and zero flux [12]. However, as some recent comparative studies have shown [13]–[16], none of these sensors have really met all the requirements above listed in one device. A large bandwidth from dc [17] to several megahertz (MHz) has been the most difficult objective, but is also one of the most crucial characteristics for modern current controlled converters having switching frequencies up to 1 MHz and fast dynamics [18], [19]. Accuracy and low cost of the sensing device are important requirements for current controlled converters. They are particularly crucial for direct pulsewidth modulation, such as hysteresis and direct power control, or for current sensor-based active ripple filters [20]. To circumvent these issues, many *sensorless* control techniques for converters and drives have been developed over

recent years [21]. Another important aspect is the immunity of the sensor against external fields. For instance, a current sensor that is physically located near a SiC J-FET, can be affected severely by dv/dt transients up to several tens of $kV/\mu s$ [22]. The parasitic coupling associated with the sensor itself can couple these transients into the sensing part causing distortion in the output. The sensor presented herein uses a planar current transformer (CT) as the main sensing device. For a high upper bandwidth limit, the parasitic capacitance and leakage inductance must be small [23]. The number of turns on the sensing coil can therefore be reduced, which also decreases the value of the magnetizing inductance (see L_{m1} in Fig. 17), thus providing some advantages [20]. The realization cost is lower for a planar transformer rather than a wire wound device.

The drawback of this solution is that the lower corner frequency increases with fewer turns. This also happens when core materials with low permeability, a gapped or core-less transformers are used. Therefore, in order to extend the bandwidth to dc while keeping the advantages at high frequency, another device able to sense the dc and low-frequency part of the measured signal can be combined with the CT. The technique of matching the frequency characteristics of two sensing devices for broad band current sensing from dc to several MHz has already been proposed in literature [5], [11], [24]–[26]. The proposed sensor features a Hall-effect based element for performing the low-frequency current sensing. There are at least three well-known architectures for combining a Hall-effect sensor and a magnetic core:

- 1) open loop;
- 2) closed loop;
- 3) a combination of open loop and CT.

For all three, the Hall element is physically inserted into a gapped magnetic structure [see Fig. 1(a), (b), and (d)]. A description of each architecture is given in [13]. Closed-loop devices are most common and operate on the principle of compensating the low-frequency flux in the core with a feedback from a dc to low-frequency sensor [25], [27], which is typically a Hall element. Since the magnetic core for a closed-loop transducer operates at zero-flux, the operating point of the sensor is also around the zero flux crossing. It is therefore unnecessary for the dc to low-frequency sensor to be linear.

The proposed transducer uses a linear Hall element for sensing the current components from dc up to the lower corner frequency of the planar CT. The measured current signal is provided by the sum of the output signal of the Hall element and the CT [see Fig. 1(d)]. Contrary to the closed-loop technology, the proposed solution is passive and does not require feedback or process electronics. As described in detail in the following sections, the matching between the Hall element and the CT is

Manuscript received February 2, 2006; revised July 10, 2006. Recommended for publication by Associate Editor E. Santi.

L. Dalessandro and J. W. Kolar are with the Power Electronic Systems Laboratory, Swiss Federal Institute of Technology (ETH) Zurich, Zurich CH-8092, Switzerland (e-mail: dalessandro@lem.ee.ethz.ch; kolar@lem.ee.ethz.ch).

N. Karrer is with the High Voltage Laboratory, Swiss Federal Institute of Technology (ETH) Zurich, Zurich CH-8092, Switzerland (e-mail: nkarrer@eeh.ee.ethz.ch).

Color versions of one or more of the figures in this paper are available online at <http://ieeexplore.ieee.org>.

Digital Object Identifier 10.1109/TPEL.2007.904198

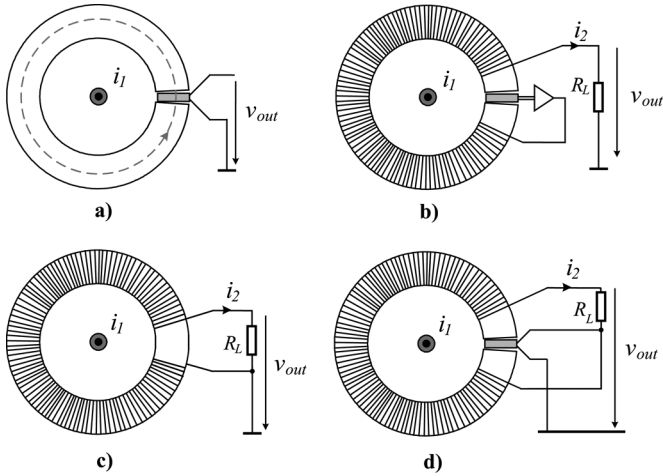


Fig. 1. Current sensors technologies based on magnetic core: (a) open loop, (b) closed loop, (c) CT, and (d) the proposed current sensor.

provided without electronics stage, which is usually required for instance in [5]. This paper presents a planar prototype of the CT that is an improvement of a previous toroidal device [23]. It has been empirically verified that the main characteristics of the dc-planar CT are:

- 1) frequency bandwidth from dc up to 30 MHz;
- 2) 40-A (dc) current rating;
- 3) high dv/dt immunity;
- 4) thermal stability (linear behavior under temperature variations);
- 5) compact planar transformer with a multilayer PCB winding;
- 6) low realization cost.

II. PRINCIPLE OF OPERATION

The driving quantity for the functioning of the sensor is the magnetic flux ϕ . This is because the output signal of the Hall-effect sensor is proportional to the flux and the output voltage of the CT is dependent on the flux rate (see Fig. 4). For this aim, it is opportune to use an equivalent circuit of the transformer which allows to calculate easily the flux and includes also the properties of the magnetic core. The capacitance-permeance analogy based model was chosen. The definitions of the used quantities along with the complete set of transformer's equations are included in the Appendix. We recall hereafter only the formulas needed to explain the principle of operation of the sensor. A sketch of the gapped CT is shown in Fig. 2. The flux in the core if $\Lambda_g \ll \Lambda_m$ is defined as

$$\phi = \Lambda_g(N_1 i_1 - N_2 i_2). \quad (1)$$

The primary and secondary voltages are given, respectively, by

$$v_1 = R_1 i_1 + L_{\sigma 1} \frac{di_1}{dt} + L_{m1} \frac{di_{m1}}{dt} \quad (2)$$

and

$$v_2 = R_2 i_2 + L_2 \frac{di_2}{dt} - M \frac{di_1}{dt} = -i_2 R_L. \quad (3)$$

From (3), the current ratio can be extracted using the Laplace transform, where s indicates the Laplace operator. The ratio

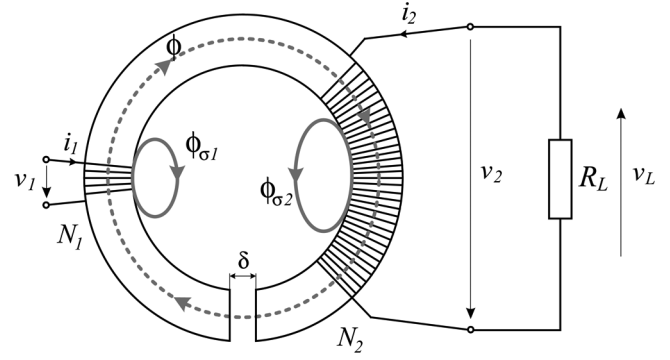


Fig. 2. Sketch of a gapped CT.

between primary and secondary currents is then provided by

$$\frac{I_2(s)}{I_1(s)} = \frac{N_1}{N_2} \frac{s \frac{L_{m2}}{R_2 + R_L}}{1 + s \frac{L_2}{R_2 + R_L}}. \quad (4)$$

A. Ideal Sensor

If the leakage inductance $L_{\sigma 2}$ is sufficiently small, which is typical for planar transformer, then

$$L_2 \approx L_{m2} \quad (5)$$

and, if the winding resistance R_2 is negligible with respect to the load resistor R_L , then the time constant associated with the secondary winding assumes the form

$$\tau = \frac{L_2}{R_L}. \quad (6)$$

Accordingly, the current ratio (4) can be written as

$$\frac{I_2(s)}{I_1(s)} = \frac{N_1}{N_2} \frac{s\tau}{1 + s\tau}. \quad (7)$$

The expression of the flux ϕ in the frequency domain is obtained from (1) and (7) as

$$\begin{aligned} \Phi(s) &= \Lambda_g(N_1 I_1 - N_2 I_2) \\ &= N_1 \Lambda_g \left(1 - \frac{N_2 I_2}{N_1 I_1} \right) I_1 \\ &= N_1 \Lambda_g \left(\frac{1}{1 + s\tau} \right) I_1. \end{aligned} \quad (8)$$

The Hall-effect element measures the dc to low-frequency components of the current i_1 . It uses the magnetic flux density B , defined as

$$B(s) = \frac{\Phi}{A} \quad (9)$$

generated by the current i_1 , to deflect an "internal" current flowing through a conductor, thus developing a transversal potential. The output voltage signal of the Hall-effect element V_H is thus proportional to B through the sensitivity S_{Hall} , measured in V/T, and is given by

$$V_H = S_{\text{Hall}} B. \quad (10)$$

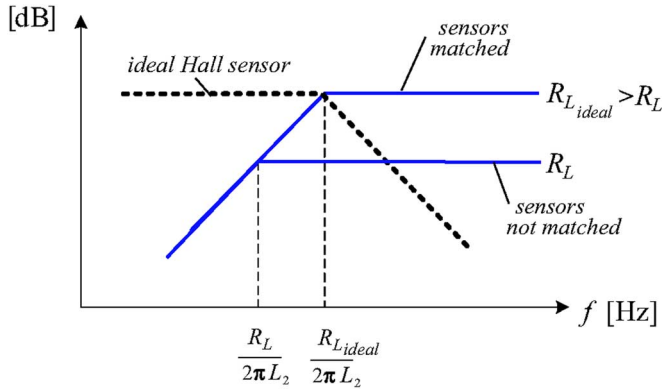


Fig. 3. Resulting transfer function of the proposed transducer. The matching between the two sensors is achieved by using an opportune value of the transformer's load resistor R_L (15).

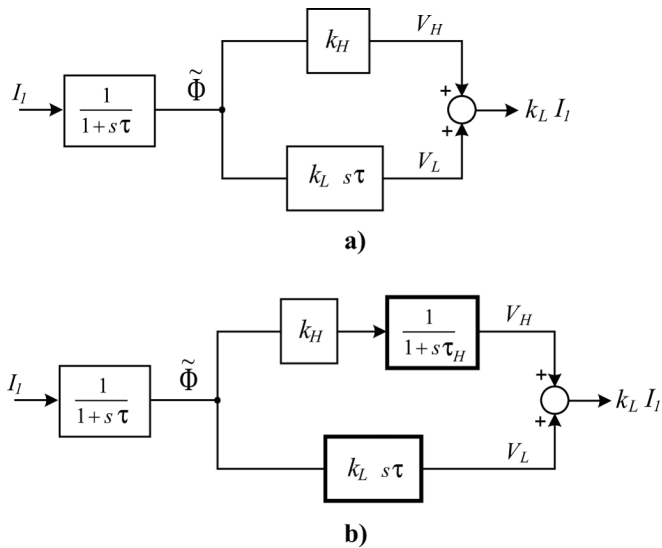


Fig. 4. Block diagrams explaining the functioning of the proposed current sensor in the frequency domain when $k_H = k_L$: (a) ideal and (b) real operating.

The transfer function (TF) of the Hall captor V_H/I_1 can finally be derived by substituting (8) and (9) in (10) and assuming $N_1 = 1$:

$$\begin{aligned} \frac{V_H}{I_1} &= \frac{\mu_0}{\delta} S_{\text{Hall}} \left(\frac{1}{1+s\tau} \right) \\ &= k_H \left(\frac{1}{1+s\tau} \right). \end{aligned} \quad (11)$$

On the other side, V_L/I_1 is the TF of the CT derived by (4)

$$\begin{aligned} \frac{V_L}{I_1} &= \frac{R_L}{N_2} \frac{s\tau}{1+s\tau} \\ &= k_L \frac{s\tau}{1+s\tau}. \end{aligned} \quad (12)$$

Let observe that (11) is a low-pass function and the (12) a high pass function having the same corner frequency as depicted in Fig. 3.

In the proposed current sensor, the output signal is provided by

$$V_{\text{out}} = V_L + V_H \quad (13)$$

and these voltages are summed without using process electronics [see Fig. 1(d)]. If the gain values of the sensor components are designed to be equal, then the overall transfer function of the sensor, provided by the sum of (11) and (12) is a flat response over the entire frequency band (see Fig. 3). Constraining the gain of each of the two transfer functions to be equal in value yields

$$\frac{R_L}{N_2} \equiv \frac{\mu_0}{\delta} S_{\text{Hall}}. \quad (14)$$

If the parameters N_2 , S_{Hall} and δ have already been selected, then the value of the load resistance R_L has to be chosen such that

$$R_L = \frac{N_2 \mu_0 S_{\text{Hall}}}{\delta} \quad [\Omega]. \quad (15)$$

In Fig. 4(a), the block diagram that explains the functioning of the sensor is shown. There, a quantity proportional to the flux $\tilde{\Phi}$ drives both the Hall-effect element and the CT, whose output signals, V_H and V_L , are summed to provide in output a constant gain equal to

$$V_{\text{out}} = k_L I_1. \quad (16)$$

B. Real Sensor

The ideal functioning of the sensor has been derived under the assumption of constant sensitivity of the Hall captor (10). Actually, the Hall sensor is better characterized by a low-pass function as

$$V_H = \frac{S_{\text{Hall}}}{1+s\tau_H} B \quad (17)$$

where τ_H is the time constant of the device. The block diagram that describes the real functioning of the sensor is depicted in Fig. 4(b). If the Hall element corner frequency f_H

$$f_H = \frac{1}{2\pi\tau_H} \quad (18)$$

is at least one decade larger than the CT's lower corner frequency f given by

$$f = \frac{1}{2\pi\tau} = \frac{R_L}{2\pi} \frac{\delta}{\mu_0 N_2^2 A} \quad (19)$$

such that the condition

$$f_H \gg f \quad (20)$$

is verified, then matching between the output signals of Hall element and CT occurs correctly, similar to the matching behavior presented in [28]. Eq. (20) ensures that the Hall-element operates in the linear part of its characteristic curve and that no further attenuation occurs by the matching point.

In case

$$\tau_H \approx \tau \quad (21)$$

then the Hall captor output signal is affected by delay, as shown in the simulation in Fig. 5(a) and in the measurement Fig. 5(b), and the sum between the signal components of Hall and CT does not reproduce properly the current step. Therefore, the values

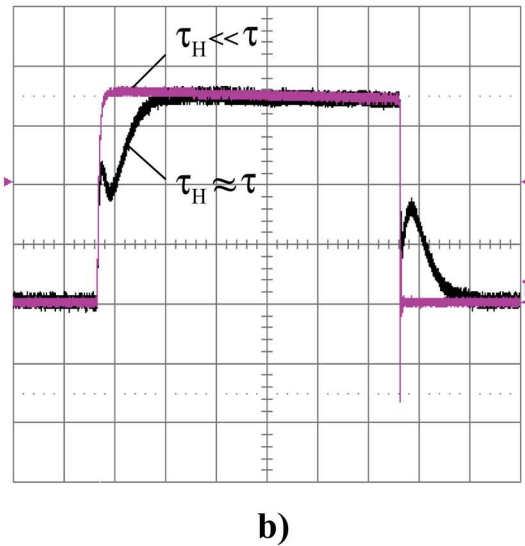
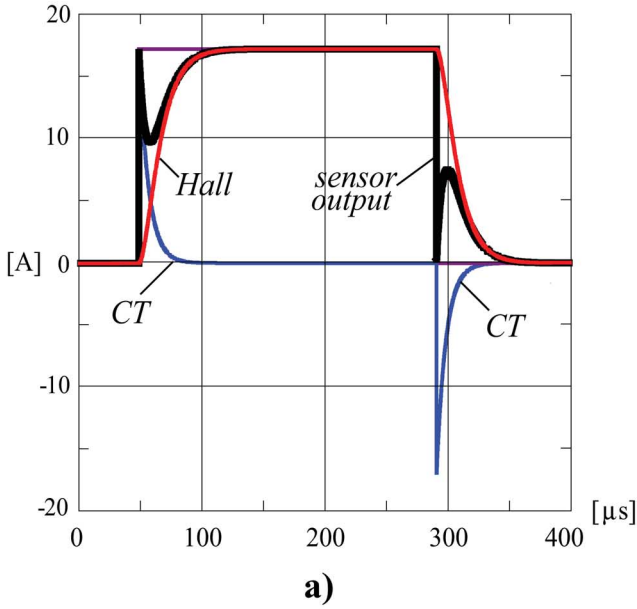


Fig. 5. Sensor components that contribute to the formation of the current step; operating principle according to Fig. 4(b). The sum between the Hall captor and the CT output signals does not reproduce properly the step because $\tau_H \approx \tau$: (a) simulation and (b) measurement.

of R_L and L_2 must be selected carefully to obtain a corner frequency f sufficiently smaller than f_H .

Moreover, the parameters $L_{\sigma 2}$ and R_2 affect the real operating of the sensor and it is opportune to include them in design and model. Although a planar transformer shows a smaller leakage inductance than a toroidal device, the $L_{\sigma 2}$ plays an increasing role at high frequency and it determines with the winding self capacitance C the upper bandwidth limit of the transformer. The value of winding resistance R_2 is dependent on the cross-section of the secondary turns; although a compact secondary coil is desirable to obtain a small device, a larger wire cross-section ensures a lower winding resistance, hence a lower corner frequency f , (19).

In a previous work, a high-frequency permeance based model of the CT was presented [23]. Here, since the matching between

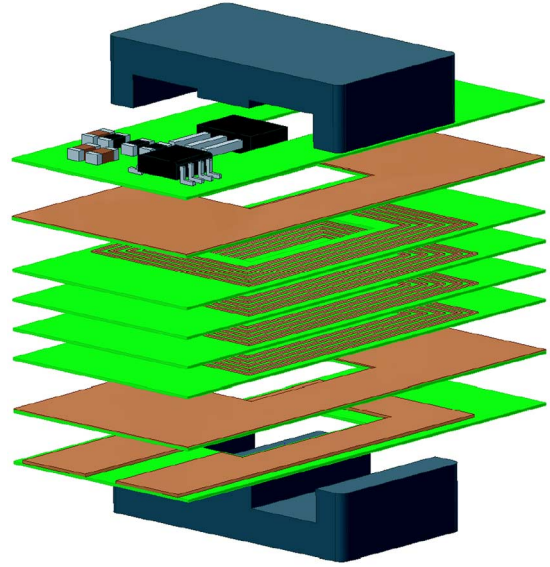


Fig. 6. Exploded drawing of the dc planar-CT indicating the placement of the layers.

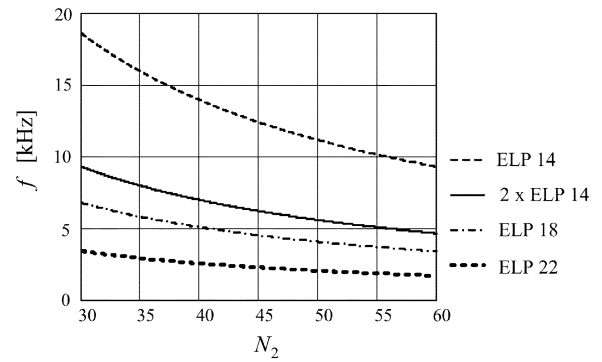


Fig. 7. Dependency of the planar CT's lower corner frequency f according to (19) on the number N_2 of secondary turns for different ELP cores.

the TF of the two sensor components occurs in the kHz range, the presented low-frequency model of the transformer is suitable for analyzing the proposed signal matching. Accordingly, skin and proximity effects in the windings, rotational magnetic losses and the secondary winding self capacitance have been neglected.

III. REALIZATION OF THE PROTOTYPE

A toroidal prototype of the proposed current sensor was shown in [23]. The device was made out of a toroidal gapped magnetic core and a Hall element positioned in the air gap. An electric screen between the primary was used to split the interwinding capacitance and to decrease the value of the leakage inductance [29]. The choice of the planar shape rather than the toroidal one leads to a significant improvement of the frequency behavior of the device and brings with it the following advantages while still retaining all the features of the toroidal prototype:

- 1) a low profile;
- 2) an embedded primary conductor in the component, and better control over parasitics;
- 3) better manufacturability;

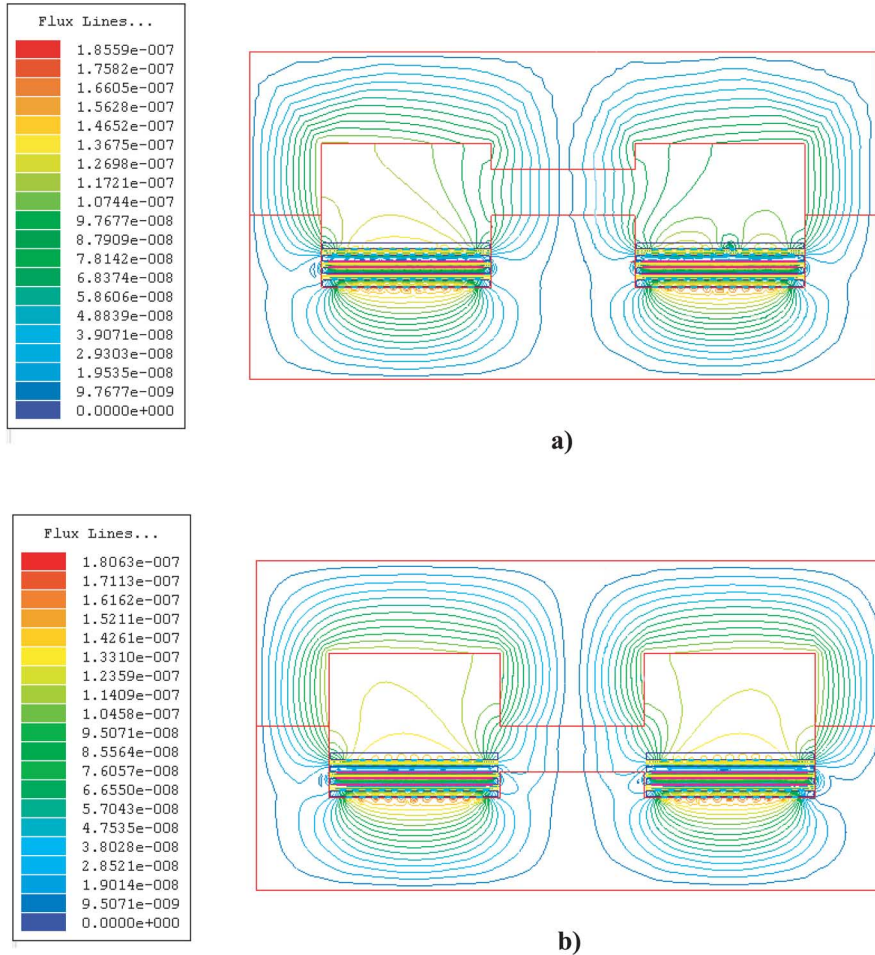


Fig. 8. Magnetic flux lines distribution within the core for a frequency of 1 kHz. This frequency corresponds to the end of the operating region of the Hall element and the beginning of the transformer's one. It is important that the flux lines are linked with the Hall element and remain within the air gap. Therefore, the solution (a) of having the air gap far from the winding-PCB layer is more convenient than having the air gap aligned with the winding PCB (b).

- 4) the ability to integrate all the main parts, i.e., windings, EM screens, process electronics into a compact and mechanically robust device;
- 5) higher frequency bandwidth.

With these aims in mind, a planar magnetic core in combination with an eight-layers PCB was built: four layers host the secondary coil of 45 turns, one layer for the primary, one for the output stage electronics, and the remaining two layers for ground plane and screen. An exploded view of the sensor structure is shown in Fig. 6. The core consists of two E-cores with an air gap of 1.4 mm. In order to design a sufficiently compact planar prototype, the smallest commercial ELP ferrite cores were selected [30]. They are ELP14, ELP18 and ELP22. To reduce the parasitics associated with the windings and to decrease the number of layers of the PCB, the number of secondary turns was selected to be the minimum possible for proper sensor operation.

For this aim, the value of the corner frequency f has been calculated as a function of the number N_2 of secondary turns for four different planar cores. The results of the calculations are shown in the curves of Fig. 7. Since a sufficient large value of the inductance L_2 is desired in order to fulfill (20), the solution of taking two ELP14 cores has also been considered. An Allegro

A3515 Hall element [31] was chosen for its linear characteristic up to 30 kHz. Therefore, only two cores, ELP18 and ELP22, with a number of turns larger than 40 fulfill (20) and present lower corner frequencies below 5 kHz. Moreover, it is important that the flux lines link the Hall element and remain within the cross-section of the air gap until the CT start working within the linear part of its frequency characteristic: this has been verified by FEM simulations shown in Fig. 8.

On the basis of these considerations, 18 different prototypes were built, with different combinations of winding strategies and layers arrangements. A photograph of the proposed dc planar-CT that features a ELP18 planar core is shown in Fig. 9.

IV. EXPERIMENTAL RESULTS

A. Current Step Response

A rectangular-shaped current waveform contains more harmonic components than other waveforms, for instance a triangular one, and is therefore a very effective test for a current sensor. The current step response of the proposed dc-planar CT was compared with three other wide-bandwidth devices: a Tektronix A6312 probe (100 MHz), a Shunt LEM 25/10 (10 MHz), and a HOKA Probe (50 MHz) [5]. The experimental

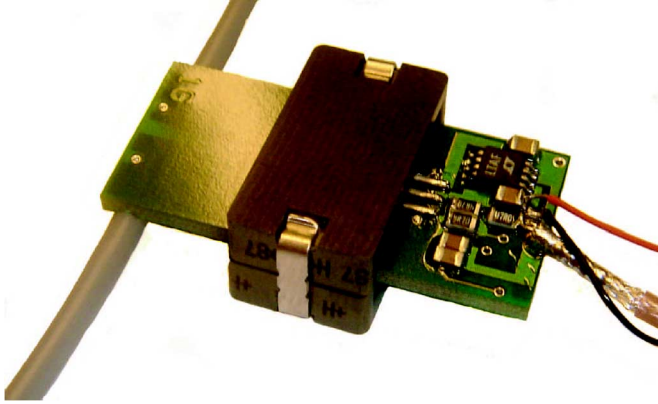


Fig. 9. Photograph of the proposed dc planar-CT featuring a planar ELP18 core.

setup is described in [28]. The measurement results are shown in Figs. 10–12, and the performance of the proposed sensor compares equally well to the other more expensive and well known current transducers. The high upper bandwidth limit of the CT measured 30 MHz according to the procedure presented in [23], and allows faithful reproduction of the rising and falling edges of the current step (see Figs. 10–11) while the Hall-element detects the stationary edges of the signal.

B. Core Saturation

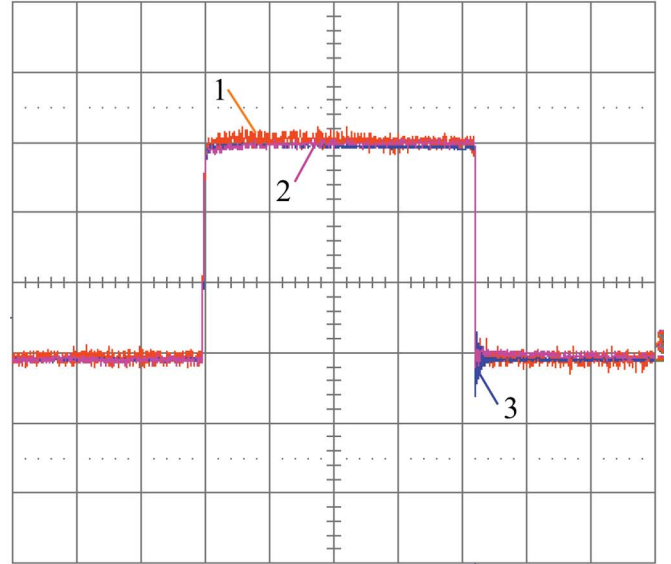
A closed-loop implementation of the sensor ensures that the magnetic core saturates at higher rating of primary current than an open-loop architecture. For a closed-loop sensor, the magnetic field in the core is compensated by the feedback action of the dc to low-frequency sensor whose output signal is injected in the secondary winding to oppose the primary MMF [see Fig. 1(b)]. If the primary current i_1 is stationary (dc) or not sufficiently compensated by the effect of the secondary current, there is no flux rate, hence the CT is inhibited and does not provide any output signal.

An issue for the proposed sensor is the saturation of the magnetic core, since no compensation loop is implemented. However, the quite large air-gap, necessitated by the physical dimensions of the Hall element, reduces the effects of the nonlinear magnetic characteristic of the core and stabilizes the value of the inductance L_{m1} . This latter becomes less dependent from the core parameters, (31), and decreases in value, because the equivalent permeability of the gapped system is smaller than the core permeability.

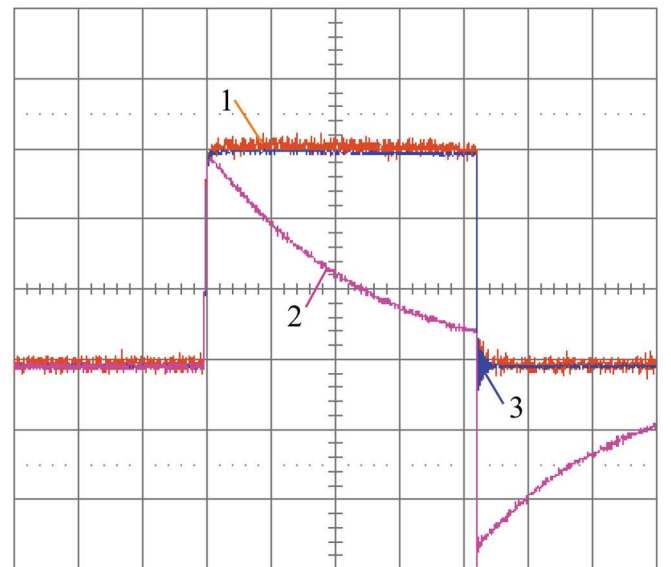
Since the volt-seconds necessary to saturate a magnetic circuit (starting from $B = 0$) are

$$\begin{aligned}\varphi_S &= N_1 B_S A \\ &= L_{m1} i_S\end{aligned}\quad (22)$$

increasing the air-gap length reduces the inductance value according to (30) and (31), whereas the current i_S , for which saturation occurs, increases. φ_S and B_S indicate saturation flux and induction, respectively. Fig. 12 shows a 0.2-ms current step of 50 A in amplitude; the sensor is able to measure such current steps. By means of similar tests, an excellent linear behavior has been registered up to 40-A dc.



a)

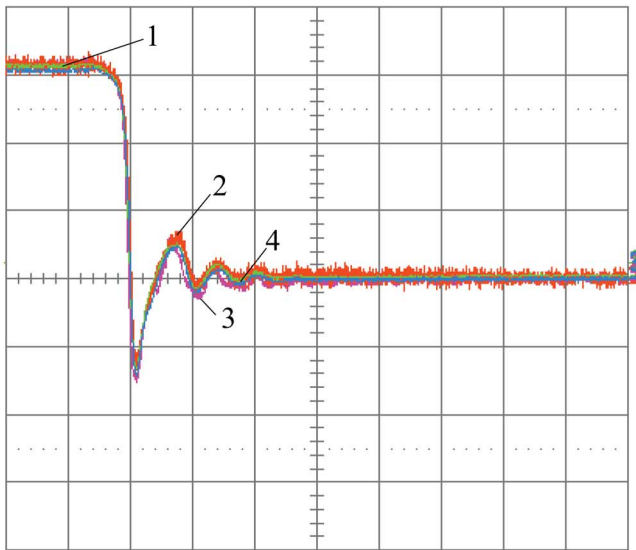


b)

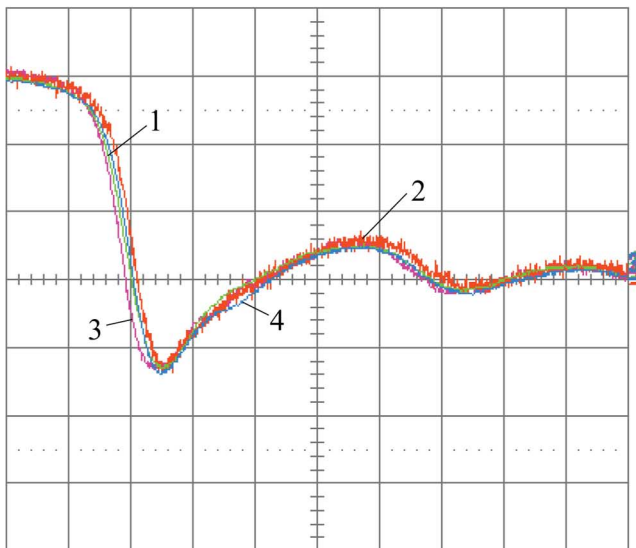
Fig. 10. (a) Current step response where the sensors are, respectively: 1) Shunt LEM 25/10, 2) proposed dc planar-CT current sensor, (3) Tektronix A6312 Probe. Vertical scale 5 A/div, time scale 50 μ s/div. In (b), the Hall sensor signal is not present; only the planar CT is sensing.

C. dv/dt Immunity Test

The interwinding capacitance of the CT couples the primary and secondary windings. Whenever there is a high dv/dt in the primary or near the secondary, the disturbance is transferred to the secondary in the form of a common mode current. This disturbance can also appear, if the current sensor is placed closely to a fast switching MOSFET: the sensor is stressed with severe dv/dt . In this case, v represents the drain to source voltage. One measurement result of dv/dt immunity is shown in Fig. 13. The measurement setup adopted to produce the voltage step was similar to the one used to generate the current step. However, a faster switching FET was used and a series connection of resistors of



a)



b)

Fig. 11. Current step response where the sensors are respectively: 1) Shunt LEM 25/10, 2) Tektronix A6312, 3) proposed dc planar-CT current sensor, 4) HOKA sensor [5]. Vertical scale 5 A/div, time scale: (a) 0.5 μ s/div, (b) 0.1 μ s/div. Furthermore, (b) shows 20-ns delay of the Tek probe.

total 3 k Ω was inserted in the primary to reduce the flowing current in the primary to nearly zero as well as the stray capacitance of the resistors. In this way, the current measured by the sensors under test was due just to the parasitic capacitances that couple the transients dv/dt into the output of the sensor. The distortion registered in output of the proposed sensor for 16 kV/ μ s voltage rate is comparable to the performance of a Tektronix A6312 used as reference device (see Fig. 13).

V. CONCLUSION

This paper has presented a novel isolated current sensor made out of the combination of a Hall-effect element, positioned in

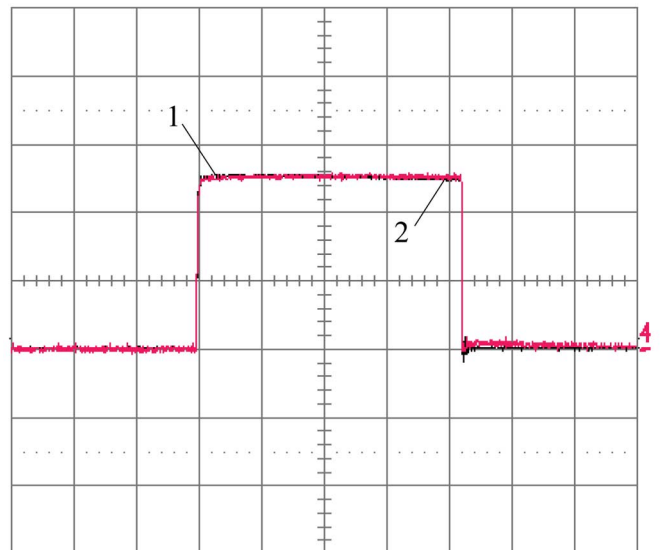


Fig. 12. Current step response where the sensors are respectively: 1) proposed dc planar-CT current sensor, 2) Shunt LEM 25/10. Vertical scale 20 A/div, time scale: 50 μ s/div.

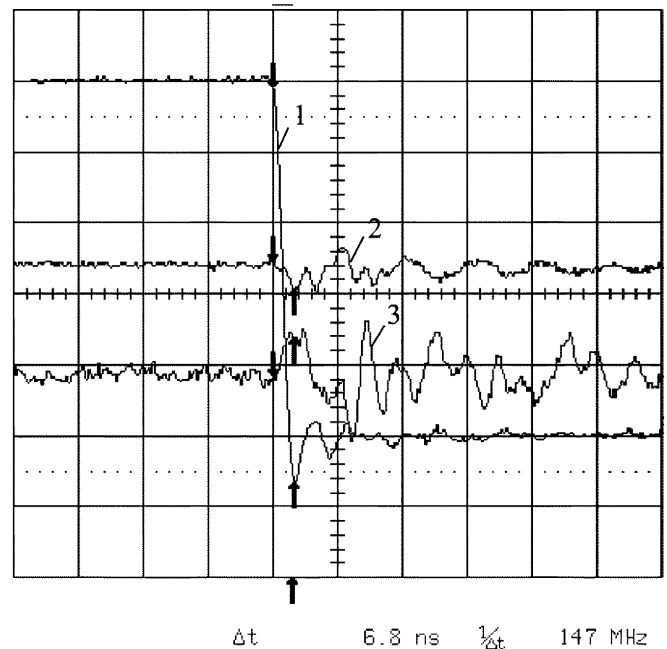


Fig. 13. dv/dt immunity test. 1) voltage step (16 kV/ μ s), 2) proposed dc planar-CT current sensor, 3) Tektronix A6312. Time scale: 20 ns/div; voltage scale: 20 V/div; current scale: 0.5 A/div.

the air gap of the magnetic structure, and a planar CT with a multilayer PCB winding. The Hall sensor is sensitive to the dc and to the low-frequency components of the measured current, whereas the higher frequencies, to which the Hall sensor is insensitive, are detected magnetically by the CT. The matching between the Hall element and the CT is performed without electronic stage.

The functioning has been explained analytically by means of a permeance-based model of the transformer. This model allows access to the flux, flux rate, and MMF, besides the electrical

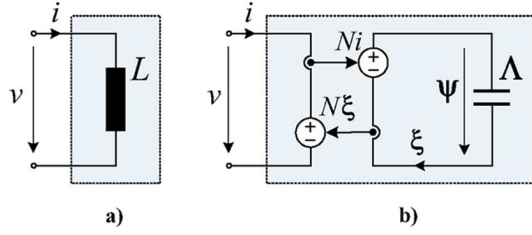


Fig. 14. Electrical circuitual model of a coil: (a) conventional equivalent and (b) permeance-capacitance analogy-based model with coupling between electrical and magnetic circuits using a Tellegen gyrator.

quantities. Furthermore, it allows time and frequency simulations on electrical network simulators of electro-magnetic networks; it allows implementation of frequency-dependent components, complex permeability, and direct core losses extraction.

Simulations and FEM results have been presented for verification. It has been shown that the appropriate dimensioning of the magnetic system, and especially the accurate selection of the corner frequency f of the CT transfer function is important to grant the correct functioning of the sensor.

The choice of the planar magnetic structure led to the following advantages, while still retaining all the features of a former toroidal prototype [23]: higher frequency bandwidth, low profile, better manufacturability, and compatibility with integration processes.

Furthermore, a planar prototype has been shown and the following features have been verified experimentally: frequency bandwidth from dc up to 30 MHz, high current rating (40-A dc), superior linearity, and high immunity against dv/dt transients.

All of these performances, in particular accuracy and low realization cost, comply with the requirements necessary for the application of the sensor within the latest generation of converters and drives.

APPENDIX

The conventional electrical equivalent of a coil is shown in Fig. 14(a), where i and v are the current and voltage at the winding terminals related by

$$v = L \frac{di}{dt} \quad (23)$$

and L is the self-inductance value. In order to highlight the properties of the core, we recall the relations

$$\begin{aligned} v &= N\xi \\ \psi &= Ni \end{aligned} \quad (24)$$

being N the number of turns, ξ the induced voltage per turn, and ψ the magnetomotive force (MMF). It should be noted that the equations (24) represent the Faraday's and Ampere's Laws, respectively [34, p.186].

Greek letters indicate the magnetic quantities to better distinguish them from the electric ones. The permeance Λ of the magnetic core is defined as

$$\Lambda = \frac{\phi}{\psi} = \frac{\mu A}{l} \quad (25)$$

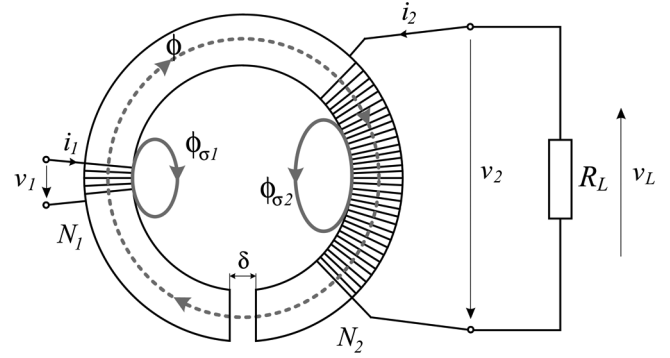


Fig. 15. Sketch of a gapped CT.

where μ is the core permeability, A and l the core cross-section and the magnetic-flux pathlength, respectively. The relation between the MMF ψ and the magnetic flux ϕ in a magnetic system

$$\xi = \frac{d\phi}{dt} = \Lambda \frac{d\psi}{dt} \quad (26)$$

can be written analogous to the relation between charge q and voltage v across a capacitor

$$i = \frac{dq}{dt} = C \frac{dv}{dt}. \quad (27)$$

From (26) and (27), it follows that the MMF ψ is used analogous to the voltage v , whereas the induced electromotive force (e.m.f.) ξ is used analogous to the electrical current i .

Accordingly, the magnetic circuit can be modelled by an electrical loop [see Fig 14(b)] where the permeance Λ is modelled by a capacitor, the current flowing is the flux rate ξ (26) and the voltage across the capacitor is the MMF ψ . The magnetic and the electric circuits are coupled by a Tellegen gyrator defined by the relations (24).

This model based on the permeance-capacitance analogy [23], [32] presents numerous advantages:

- 1) the implementation of frequency dependent components and complex permeability;
- 2) the simulation of a magnetic network by an electrical circuit;
- 3) it allows access to the flux rate ξ and the MMF ψ ;
- 4) geometry and number of turns are included in the model;
- 5) since a resistance element in the permeance model represents core losses (unlike the conventional magnetic reluctance model where resistance represents energy storage), core losses could be also extracted using this method [23].

Fig. 15 depicts a sketch of a gapped CT comprised of N_1 and N_2 primary and secondary turns of resistance R_1 and R_2 , respectively, a load resistor R_L , and a gapped magnetic core, of air-gap δ , cross-sectional area A , and flux pathlength l in the core.

The transformer equivalent model shown in Fig. 16 has been drawn using the capacitance-permeance analogy. All the set of equations that describe a transformer can be written by inspection of the circuit in Fig. 16.

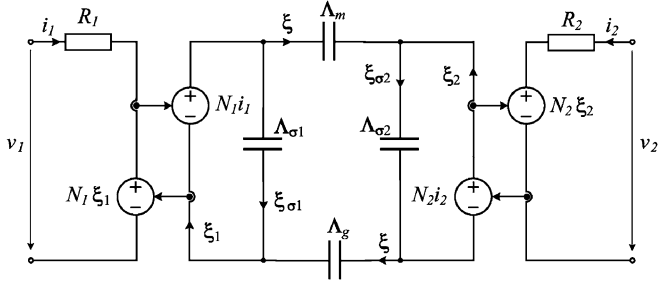


Fig. 16. Equivalent model of a transformer based on the permeance-capacitance analogy. In particular, Λ_m and Λ_g indicate the permeances of the magnetic core and the air-gap, respectively; $\Lambda_{\sigma 1}$ and $\Lambda_{\sigma 2}$ the shunt permeances of the primary and secondary leakage fluxes.

Accordingly, the equations of the electric loops are

$$\begin{aligned} v_1 &= R_1 i_1 + N_1 \xi_1 = R_1 i_1 + N_1 \frac{d\phi_1}{dt} \\ v_2 &= R_2 i_2 + N_2 \xi_2 = R_2 i_2 + N_2 \frac{d\phi_2}{dt} \end{aligned} \quad (28)$$

whereas the relations associated to the nodes of the magnetic circuit are

$$\begin{aligned} \phi_1 &= \phi_{\sigma 1} + \phi \\ \phi_2 &= \phi_{\sigma 2} - \phi \end{aligned} \quad (29)$$

and

$$\begin{aligned} \phi_{\sigma 1} &= \Lambda_{\sigma 1} N_1 i_1 \\ \phi_{\sigma 2} &= \Lambda_{\sigma 2} N_2 i_2 \\ \phi &= \left(\frac{\Lambda_m \Lambda_g}{\Lambda_m + \Lambda_g} \right) (N_1 i_1 - N_2 i_2). \end{aligned} \quad (30)$$

The primary and secondary leakage fluxes, $\phi_{\sigma 1}$ and $\phi_{\sigma 2}$, are dependent on the permeances $\Lambda_{\sigma 1}$ and $\Lambda_{\sigma 2}$ of the leakage paths whereas the magnetizing flux ϕ is proportional to the resultant MMF and to the permeance of the air gap Λ_g , which is much smaller than the core permeance Λ_m

$$\Lambda_g = \frac{\mu_0 A}{\delta} \ll \frac{\mu_0 \mu_r A}{l} = \Lambda_m \quad (31)$$

where μ_0 and μ_r air and core permeability, respectively. By substituting (29) and (30) in (28) and considering (31), the primary voltage v_1 is given by

$$\begin{aligned} v_1 &= R_1 i_1 + N_1 \frac{d\phi_{\sigma 1}}{dt} + N_1 \frac{d\phi}{dt} \\ &= R_1 i_1 + \Lambda_{\sigma 1} N_1^2 \frac{di_1}{dt} \\ &\quad + \Lambda_g N_1^2 \frac{di_1}{dt} - \Lambda_g N_1 N_2 \frac{di_2}{dt} \end{aligned} \quad (32)$$

where

$$\begin{aligned} L_{\sigma 1} &= \Lambda_{\sigma 1} N_1^2 \\ L_{m1} &= \Lambda_g N_1^2 \\ M &= \Lambda_g N_1 N_2 \\ L_1 &= L_{\sigma 1} + L_{m1} \end{aligned}$$

are *leakage*, *magnetizing*, *mutual*, and *self*-inductances, respectively, of the primary winding. L_1 and M can be measured, L_{m1} can be calculated and $L_{\sigma 1}$ can be derived. These parameters

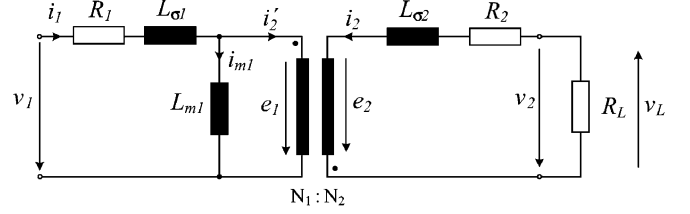


Fig. 17. Equivalent electric circuit of a CT.

can be determined by means of the well known open-circuit and short-circuit tests [33]. (32) can be further arranged as follows:

$$\begin{aligned} v_1 &= R_1 i_1 + L_{\sigma 1} \frac{di_1}{dt} + L_{m1} \frac{d}{dt} \left(i_1 - \frac{N_2}{N_1} i_2 \right) \\ &= R_1 i_1 + L_{\sigma 1} \frac{di_1}{dt} + L_{m1} \frac{di_{m1}}{dt} \end{aligned} \quad (33)$$

which corresponds to the primary side of the electrical circuit in Fig. 17. There, the currents i'_2 and i_{m1} are defined, respectively, as

$$i'_2 = \frac{N_2}{N_1} i_2 \quad (34)$$

$$i_{m1} = i_1 - i'_2. \quad (35)$$

In a similar fashion, the output voltage v_2 can be written from (28) and (29) as

$$v_2 = R_2 i_2 + N_2 \frac{d\phi_{\sigma 2}}{dt} - N_2 \frac{d\phi}{dt} \quad (36)$$

and the *leakage*, *magnetizing*, *mutual*, and *self*-inductances of the secondary winding can be defined analogous to the primary as follows:

$$\begin{aligned} L_{\sigma 2} &= \Lambda_{\sigma 2} N_2^2 \\ L_{m2} &= \Lambda_g N_2^2 \\ M &= \Lambda_g N_2 N_1 \\ L_2 &= L_{\sigma 2} + L_{m2}. \end{aligned}$$

The e.m.f. e_2 induced in the secondary by the mutual flux ϕ is defined as

$$e_2 = N_2 \frac{d\phi}{dt} \quad (37)$$

and it drives the secondary current i_2 . The e.m.f. e_1 induced across the primary winding is similarly given by

$$\begin{aligned} e_1 &= N_1 \frac{d\phi}{dt} \\ &= L_{m1} \frac{di_{m1}}{dt} \end{aligned} \quad (38)$$

and it is related to e_2 through the transformer ratio

$$\frac{e_2}{e_1} = \frac{N_2}{N_1}. \quad (39)$$

This latter and (34) constitute the equations of an ideal transformer, i.e., core permeability μ_r infinite and magnetic flux ϕ zero. Equation (36) can be written as

$$e_2 = R_2 i_2 + L_{\sigma 2} \frac{di_2}{dt} - v_2. \quad (40)$$

Let us define R_L and v_L as the load resistor and load voltage

$$\begin{aligned} v_L &= R_L i_2 \\ &= -v_2. \end{aligned} \quad (41)$$

Considering (35), (38), (39), and (41), it follows that

$$\begin{aligned} \frac{N_2}{N_1} \left(L_{m1} \frac{d}{dt} \left(i_1 - \frac{N_2}{N_1} i_2 \right) \right) &= R_2 i_2 + L_{\sigma 2} \frac{di_2}{dt} + v_L \\ M \frac{di_1}{dt} - L_{m2} \frac{di_2}{dt} &= R_2 i_2 + L_{\sigma 2} \frac{di_2}{dt} + R_L i_2 \\ M \frac{di_1}{dt} &= R_2 i_2 + L_2 \frac{di_2}{dt} + R_L i_2. \end{aligned} \quad (42)$$

Using the Laplace transform, where s indicates the Laplace operator, from (42) the ratio between primary and secondary currents is then provided by

$$\begin{aligned} \frac{I_2(s)}{I_1(s)} &= \frac{sM}{R_2 + R_L + sL_2} \\ &= \frac{N_1}{N_2} \frac{sL_{m2}}{R_2 + R_L + sL_2} \\ &= \frac{N_1}{N_2} \frac{s \frac{L_{m2}}{R_2 + R_L}}{1 + s \frac{L_2}{R_2 + R_L}}. \end{aligned} \quad (43)$$

ACKNOWLEDGMENT

The authors wish to thank Dr. W. G. Odendaal for manuscript discussion, and P. Furrer and P. Seitz for their assistance in constructing the prototypes.

REFERENCES

- [1] F. Costa, P. Poulichet, F. Mazaleyra, and E. Labouré, "The current sensors in power electronics, a review," *EPE J.*, vol. 11, pp. 7–18, Oct. 2001.
- [2] D. Y. Qiu, S. C. Yip, H. S.-H. Chung, and S. Y. R. Hui, "On the use of current sensors for the control of power converters," *IEEE Trans. Power Electron.*, vol. 18, no. 4, pp. 1047–1052, Jul. 2003.
- [3] L. A. Kojovic, "Guidelines for current transformers selection for protection systems," in *Proc. Power Eng. Soc. Summer Meeting*, 2001, pp. 593–598.
- [4] J. R. Stack, T. G. Habetler, and R. G. Harley, "Bearing fault detection via autoregressive stator current modeling," *IEEE Tran. Ind. Appl.*, vol. 40, no. 3, pp. 740–747, May/June 2004.
- [5] N. Karrer and P. Hofer-Noser, "A new current measuring principle for power electronics applications," in *Proc. Inform. Stor. Process. Conf.*, 1999, pp. 279–282.
- [6] C. Oates, A. J. Brunett, and C. James, "The design of high performance Rogowski coils," in *Proc. Power Electron., Mach. Drives Conf.*, 2002, pp. 568–573.
- [7] L. Zhao, J. D. van Wyk, and W. G. Odendaal, "Planar embedded pickup coil sensor for integrated power electronics modules," in *Proc. Appl. Power Electron. Conf.*, 2004, pp. 945–951.
- [8] G. Laimer and J. W. Kolar, "Design and experimental analysis of a DC to 1 MHz close loop magnetoresistive current sensor," in *Proc. Appl. Power Electron. Conf.*, 2005, pp. 1288–1292.
- [9] L. Di Rienzo, R. Bazzocchi, and A. Manara, "Circular arrays of magnetic sensors for current measurements," *IEEE Tran. Instrum. Meas.*, vol. 50, no. 5, pp. 1093–1096, Oct. 2001.
- [10] K. Bohnert, H. Brändle, M. G. Brunzel, P. Gabus, and P. Guggenbach, "Highly accurate fiber-optic current sensor for the electro-winning industry," *IEEE Trans. Ind. Appl.*, vol. 43, no. 1, pp. 180–187, Jan./Feb. 2007.
- [11] L. Ghislanzoni and J. A. Carrasco, "A DC current transformer for large bandwidth and high common mode rejection," *IEEE Tran. Ind. Electron.*, vol. 46, no. 3, pp. 631–636, Jun. 1999.
- [12] LEM Current Sensors 2005 [Online]. Available: www.lem.com
- [13] E. Favre and W. Teppan, "State of the art in current sensing technologies," in *Proc. Power Electron. Intell. Motion Conf.*, Nov. 2003, pp. 549–554.
- [14] C. Xiao, L. Zhao, T. Asada, W. G. Odendaal, and J. D. van Wyk, "An overview of integratable current sensors technologies," in *Proc. Power Electron. Spec. Conf.*, 2003, pp. 1252–1257.

- [15] P. Ripka, "Current sensors using magnetic materials," *Int. J. Optoelectron. Adv. Mater.*, vol. 6, pp. 587–592, Jun. 2004.
- [16] F. Costa, E. Labouré, F. Forest, and C. Gautier, "Wide bandwidth, large AC current probe for power electronics and EMI measurements," *IEEE Tran. Ind. Electron.*, vol. 44, no. 4, pp. 502–511, Aug. 1997.
- [17] H. G. Sauer, "Influence of the dc current on the operating of a current transformer," *Messen+Prüfen/Automat.*, pp. 267–275, Jun. 1975.
- [18] G. Laimer and J. W. Kolar, "Wide bandwidth low complexity isolated current sensor to be employed in a 10 kW/500 kHz three-phase unity power factor PWM rectifier system," in *Proc. Power Electron. Spec. Conf.*, 2002, pp. 1065–1070.
- [19] J. Pankau, D. Leggate, D. Schlegel, R. Kerkman, and G. Skibiniski, "High frequency modelling of current sensors," *IEEE Tran. Ind. Appl.*, vol. 35, no. 6, pp. 1374–1382, Nov.–Dec. 1999.
- [20] M. Zhu, D. J. Perreault, V. Caliskan, T. C. Neugebauer, S. Guttowski, and J. G. Kassakian, "Design and evaluation of feedforward active ripple filters," *IEEE Trans. Power Electron.*, vol. 20, no. 2, pp. 276–285, Mar. 2005.
- [21] M. P. Kazmierkowski, R. Krishnan, and F. Blabjeerg, *Control in Power Electronics*. New York: Academic, 2002.
- [22] S. Round, M. L. Heldwein, J. W. Kolar, A. Melkonyan, and I. Hofsjager, "A SiC JFET driver for a 5 kW, 150 kHz three-phase PWM converter," in *Proc. Ind. Appl. Soc. Conf.*, 2005, pp. 410–416.
- [23] L. Dalessandro, W. G. Odendaal, and J. W. Kolar, "HF characterization and non-linear modeling of a gapped toroidal magnetic structure," *IEEE Trans. Power Electron.*, vol. 21, no. 5, pp. 1167–1175, Sep. 2006.
- [24] L. Ghislanzoni, "Magnetic coupled current sensing techniques for spacecraft systems," in *Proc. Eur. Space Power Conf.*, 1989, pp. 323–327.
- [25] K. Unser, "Beam current transformers with DC to 200 MHz range," *IEEE Tran. Nucl. Sci.*, vol. NS-16, no. 3, pp. 934–938, Jun. 1969.
- [26] J. Weber, *Oscilloscope Probe Circuits*. Beaverton, OR: Tektronix, Inc., 1969.
- [27] S. Ogasawara, K. Murata, and H. Akagi, "A digital current sensor for PWM inverters," in *Proc. Ind. Appl. Soc. Conf.*, 1992, pp. 949–955.
- [28] N. Karrer, "Hochdynamische Erfassung Elektrischer Ströme über Stossfrei Verkoppelte Wandler," VDI, Düsseldorf, Germany, Rep. 946, 2002.
- [29] E. Labouré, F. Costa, and F. Forest, "Current measurement in static converters and realization of a high frequency passive current probe," in *Proc. Eur. Power Electron. Conf.*, 1993, pp. 478–483.
- [30] EPCOS Ferrites Datasheets and Specifications 2005 [Online]. Available: www.epcos.com
- [31] Allegro, MycroSystems, Inc. Linear Hall Sensors. 2005 [Online]. Available: www.allegromicro.com
- [32] R. W. Buntentbach, "Analog between magnetic and electrical circuits," *Electron. Prod.*, pp. 108–113, Oct. 1969.
- [33] A. E. Fitzgerald, C. Kingsley, and S. D. Umans, *Electric Machinery*. New York: McGraw-Hill, 2003.
- [34] C. R. Paul, *Electromagnetics for Engineers—With Applications*. New York: Wiley, 2004.



Luca Dalessandro (S'02) was born in Italy on April 29, 1978. He received the M.Sc. degree (with first class honors) in electrical engineering from the Politecnico di Bari, Bari, Italy, in 2001 and is currently pursuing the Ph.D. degree in electrical engineering at the Swiss Federal Institute of Technology (ETH) Zurich, Switzerland.

From 2001 to 2002, he was Researcher at the Max-Planck-Institute for Mathematics in the Sciences (MPI-MIS), Leipzig, Germany. From 2002 to 2006, he was a Research and Teaching Assistant at the Power Electronics Systems Laboratory (PES), ETH Zurich. In the summer of 2006, he joined the NSF Engineering Research Center for Power Electronics Systems (CPES), Virginia Polytechnic Institute and State University, Blacksburg, as a Researcher. He is also an Adjunct Faculty Member of the Bradley Department of Electrical and Computer Engineering, Virginia Tech, for which he teaches an advanced course on electromagnetic fields. His research interests include three-phase converters, electromagnetics, EMC and continuum electromechanics.

Mr. Dalessandro is a Registered Professional Engineer in Italy.



Nicolas Karrer (S'88–M'01) received the M.Sc and the Ph.D. degrees in electrical engineering from the Swiss Federal Institute of Technology (ETH), Zurich, Switzerland, in 1990 and 2001, respectively.

He was involved in an exchange program at McDonnell Douglas Corporation, Saint Louis, MS, and he held a position of Assistant at ETH Zurich. He is currently a Technical Assistant at the ETH Zurich and a Lecturer at a technical college in Winterthur, Switzerland. He also designs customized current probes for power-electronics apparatus and is starting a spin-off company. His main areas of interest are current measurement, simulations, photovoltaics, power electronics, and teaching.



Johann W. Kolar (SM'04) received the Ph.D. degree (with highest honors) in industrial electronics from the University of Technology, Vienna, Austria.

Since 1984, he has been with the University of Technology, Vienna, and has been teaching and working in research in close collaboration with international industry in the fields of high performance drives, high frequency inverter systems for process technology, and uninterruptible power supplies. He has proposed numerous novel converter topologies, e.g., the Vienna rectifier and the three-phase ac–ac sparse matrix converter concept. He has published over 200 scientific papers in international journals and conference proceedings and has filed more than 50 patents. He was appointed Professor and Head of the Power Electronic Systems Laboratory, Swiss Federal Institute of Technology (ETH), Zurich, in 2001. Since 2002, he has been an Associate Editor of the *Journal of Power Electronics* of the Korean Institute of Power Electronics and a member of the Editorial Advisory Board of the *IEEE Transactions on Electrical and Electronic Engineering*. The focus of his current research is on ac–ac and ac–dc converter topologies with low effects on the mains, e.g., for power supply of telecommunication systems, more-electric-aircraft applications, and distributed power systems in connection with fuel cells. Further main areas of research are the realization of ultracompact intelligent converter modules employing the latest power semiconductor technology (SiC), novel concepts for cooling and EMI filtering, multiphysics/multiscale simulation, pulsed power, bearingless motors, and power MEMS.

Dr. Kolar is a member of the IEEJ and of Technical Program Committees of numerous international conferences in the field (e.g., Director of the Power Quality Branch of the International Conference on Power Conversion and Intelligent Motion). From 1997 through 2000, he served as an Associate Editor of the IEEE TRANSACTIONS ON INDUSTRIAL ELECTRONICS and since 2001 as an Associate Editor of the IEEE TRANSACTIONS ON POWER ELECTRONICS.